pp 1442–1474. © Royal Aeronautical Society 2018
doi: 10.1017/aer.2018.66

Improved aerostructural performance via aeroservoelastic tailoring of a composite wing

Eduardo P. Krupa
eduardo.krupa@bristol.ac.uk

Jonathan E. Cooper, Alberto Pirrera and Raj Nangia
Department of Aerospace Engineering
University of Bristol
Bristol
UK

ABSTRACT

This paper investigates the synergies and trade-offs between passive aeroelastic tailoring and adaptive aeroelastic deformation of a transport composite wing for fuel burn minimisation. This goal is achieved by optimising thickness and stiffness distributions of constitutive laminates, jig-twist shape and distributed control surface deflections through different segments of a nominal "cruise-climb" mission. Enhanced aerostructural efficiency is sought both passively and adaptively as a means of aerodynamic load redistribution, which, in turn, is used for manoeuvre load relief and minimum drag dissipation. Passive shape adaptation is obtained by embedding shear-extension and bend-twist couplings in the laminated wing skins. Adaptive camber changes are provided via full-span trailing-edge flaps. Optimised design solutions are found using a bi-level approach that integrates gradient-based and particle swarm optimisations in order to tailor structural properties at rib-bay level and retrieve blended stacking sequences. Performance benefits from the combination of passive aeroelastic tailoring with adaptive control devices are benchmarked in terms of fuel burn and a payload-range efficiency. It is shown that the aeroservoelastically tailored composite design allows for significant weight and fuel burn improvements when compared to a similar all-metallic wing. Additionally, the trailing-edge flap augmentation can extend the aircraft performance envelope and improve the overall cruise span efficiency to nearly optimal lift distributions.

Keywords: Adaptive trailing-edge devices; fuel burn minimisation; composite wing; aeroservoelastic tailoring

Received 23 November 2017; revised 3 May 2018; accepted 8 May 2018; first published online 20 June 2018.

https://doi.org/10.1017/aer.2018.66 Published online by Cambridge University Press

NOMENCLATURE

Acronyms and Abbreviations

AoA	Angle-of-Attack
C.G.	Centre of Gravity
CFD	Computational Fluid Dynamics
CFRP	Carbon Fibre Reinforced Polymer
CRM	NASA Common Research Model
DLM	Doublet-Lattice Method
DMI	Direct Matrix Input
FE	Finite Element
MTOW	Maximum Take-Off Weight
OEW	Operational Empty Weight
PSO	Particle Swarm Optimisation
SST	Stacking Sequence Table
VCCTF	Variable Camber Continuous Trailing-Edge Flaps

Symbols

$\bar{c}$	mean aerodynamic chord
c_l	sectional lift coefficient
C	optimisation design constraints
C_L	aircraft lift coefficient
C_D	aircraft drag coefficient
C_{D_0}	wing zero-lift drag coefficient
C_{D_c}	wing wave drag coefficient
C_{D_l}	lift-induced drag coefficient
$C_{D_{\text{losses}}}$	drag coefficient due to non-modelled fuselage and vertical tail
C_{D_p}	wing profile drag
C_f	viscous drag coefficient
FB	mission fuel burn
$f_{\text{obj}}^{\text{top-level}}$	top-level optimisation objective function
$f_{\text{obj}}^{\text{bottom-level}}$	bottom-level optimisation objective function
$\mathcal{F}$	form factor
h	laminate thickness
KS	Kreisselmer-Steinhauser design constraint
M	Mach number
N_L	number of load cases
N_p	wing patch number
PRE	Payload-Range Efficiency parameter
R	design mission range
Re_x	wing average Reynolds number
S	wing planform area
S_{wetted}	wing wetted area
$TSFC$	Thrust Specific Fuel Consumption
t/c	thickness-to-chord ratio

https://doi.org/10.1017/aer.2018.66 Published online by Cambridge University Press

t_p	wing patch thickness
U_0	free-stream velocity
U_k	composite material invariants, with $k = 1, \ldots 5$
x_{t}	optimisation design variables describing thicknesses of the main wing sub-structure components
x_{comp}	optimisation design variables describing in-plane and out-of-plane lamination parameters
x_{jig}	optimisation design variables describing the wing jig-twist shape
x_{ctrl}	optimisation design variables describing trailing-edge control deflections
$(x/c)_{\max}$	chordwise maximum thickness position
W	aircraft weight
W_{wing}	half-wing structural weight
z	laminate through-thickness coordinate z; wing bending deformation
θ	laminate ply angle along the through-thickness coordinate z; wing twist
Λ_{le}	wing leading-edge sweep angle
$\Lambda_{t/c_{\max}}$	geometric sweep angle of the maximum wing thickness line
$\lambda_{\min}$	minimum buckling load factor
α_i	weighting factors for the bottom level optimisation objective function
ν	kinematic viscosity
ρ_{KS}	*KS* aggregation factor
ξ_i^j	lamination parameters, with $i = 1, \ldots 4$, and $j = A, D$
$\mathbf{x}$	vector of design variables
$\mathbf{A}$	laminate in-plane stiffness matrix
$\mathbf{B}$	laminate bending-extension coupling stiffness matrix
$\mathbf{D}$	laminate out-of-plane stiffness matrix
$\mathbf{M}$	laminate generalised moments
$\mathbf{N}$	laminate generalised forces
$\boldsymbol{\varepsilon}^{\mathbf{0}}$	laminate generalised strains
$\boldsymbol{\kappa}$	laminate generalised curvatures

Subscripts

i	i^{th} finite element; i^{th} cruise segment, i^{th} load case
Lam	laminate
MinStrain	minor principal strain
MaxStrain	major principal strain
MinStress	minor principal stress
MaxStress	major principal stress
p	wing patch number
Stress-Mises	Von-Mises stress
Strain-Mises	Von-Mises strain

1.0 INTRODUCTION

The current commercial aviation industry forecasts a market growth rate of approximately 5% yearly[1,2] and is facing challenging demands for improvements in fuel efficiency and

https://doi.org/10.1017/aer.2018.66 Published online by Cambridge University Press

greener operations (lower CO_2 emissions and reduced noise pollution). This trend is further heightened by fuel prices volatilities and random market instabilities, which are becoming crucial design drivers in today's aviation industry[1]. Despite the progress of conventional aircraft technologies over the past decades, fuel burn metrics are still found to be lagging behind the goals established by industry regulators[3], indeed is well know that the industry's performance in terms of metrics such as cost per passenger mile are still improving but at a much reduced rate. It is expected that major and drastic improvements in aircraft performance are likely to be achieved only by means of potential and prospective technological enablers – for instance, the use of novel aerodynamic, propulsion and structural concepts[4] to tackle the three elements of the well-known Breguet Range Equation that can be employed to increase aircraft performance via improved lift/drag, better specific fuel consumption and less weight.

Composites are now widely used in aircraft structures with both the B787 and A350 having over 50% of their structure consisting of composite (primarily carbon fibre reinforced polymer-CFRP) materials and this increased use has been based upon their improved strength to weight characteristics compared to metals. However, virtually all applications of composite materials have failed to take account of the anisotropic characteristics of such materials and symmetric/balanced lay-ups have been used so that the composite behave as a "black-metal". The possibilities of using composite materials to passively "tailor" the behaviour of flexible wings through coupling of the bending and torsion deflections have been known since the 1980s[5] when they were applied to the forward swept wing X-29 research aircraft[6]; however, little application of aeroelastic tailoring has been applied since then to commercial airplanes.

Passive aeroelastic tailoring approaches have proven the capability to effectively minimise wingbox structural weight, for both all-metallic and composite airframes, under a variety of static and dynamic constraints[7–10] and to reduce fuel burn of conventional transport aircraft configurations[11–15]. Recent work has considered the use of novel materials and structural concepts such as tow-steering[16–18] and topological optimised stiffening members[19–22], which have shown the ability to widen the design space offering additional ways to locally tailor the structure for enhanced aerostructural performance and simultaneously mitigate static and dynamic instabilities, such as panel buckling, gust loads and flutter.

It is anticipated that further significant aerostructural gains in aircraft performance will only be possible using non-conventional or hybrid design approaches, such as the so-called "integrated aeroservoelastic tailoring"[23], or simply, aeroservoelastic tailoring. This discipline aims to exploit the synergies between passive aeroelastic structural adaptation and active/adaptive control of aerodynamic surfaces. The expected outcome is the creation of designs that outperform those following solely passive aeroelastic tailoring paradigms. It is worth mentioning that aeroservoelastic tailoring is used here to refer to a broader context, where the control surfaces can be used not only to improve dynamic related design qualities, but also for controlling quasi-steady aerodynamic loads at symmetric manoeuvres.

The use of control surfaces for active gusts and manoeuvre loads alleviation is well established in current transport and this reduction in loads leads to a corresponding decrease in aircraft weight and also to improve ride quality[24]. Moreover, a number of recent studies have explored active aeroelastic adaptations as a means to improve aircraft overall performance. It has been shown that Variable Camber Continuous Trailing-edge Flaps (VCCTF)[25] can be rotated to optimal patterns for load relief (and thus achieving a lighter-weight wingbox) at

https://doi.org/10.1017/aer.2018.66 Published online by Cambridge University Press

symmetric and roll manoeuvres[26], and/or to improve fuel burn and to mitigate flutter[27,28] of an all-metallic variant of the NASA Common Research Model[29] subjected to stresses, buckling, flutter and actuator constraints. There has also been interest in evaluating potential benefits of trailing-edge control devices for minimum drag[30,31], particularly in cruise and in off-design conditions[32,33].

More recently, aeroservoelastic tailoring has been combined with spars and ribs topology optimisation to achieve more structurally efficient configurations of a composite flying-wing augmented with distributed trailing-edge flaps[34]. High-fidelity aerostructural optimisations including trailing-edge shape design variables were also shown to produce solutions capable of performing aerodynamically better than a traditional design across different points in the flight envelope[35,36]. Overall, these results encourage the use of aft-camber tailoring as a prospective mechanism for improving aerodynamic efficiency at a reduced structural weight of the state-of-the-art transport aircraft.

Regardless of the growing interest in improving conventional designs using aeroservoelastic tailoring approaches, the majority of work undertaken by the research community has focused only on all-metallic solutions. No formal study that compares all-metallic and composite wingboxes augmented by trailing-edge aerodynamic devices has been made, so that potential benefits of combining composite stiffness tailoring with control surface scheduling for an aeroelastic wing remains open to question. It is thought that introducing composite materials into state-of-the-art airframes can significantly widen the design options as one can take advantage of their tailoring capabilities by concurrently designing the structure, its constituent material and control devices rotation pattern for a number of design purposes.

The goal of this paper is to perform aeroservoelastic tailoring optimisation of a transport composite wing and to understand physical behaviours that govern these configurations benchmarking the optimised solutions found with similar all-metallic counterparts. In order to do so, passive shape adaptation is combined with adaptive aft-camber tailoring of the composite wingbox with 12 distributed full-span control surfaces in order to improve fuel burn in a "cruise-climb" mission. Aeroservoelastic tailoring of the representative wingbox is sought by optimising variations in thicknesses, laminate stiffnesses, jig-twist shape and control surfaces scheduling (for both cruise drag and load relief) subjected to stresses, strains, and buckling constraints. Four different optimisation problems are carried out:

i. an all-metallic wingbox with undeflected control surfaces;
ii. a wingbox with composite skins and undeflected control surfaces;
iii. an all-metallic wingbox augmented by distributed control surfaces and;
iv. a wingbox with composite skins augmented by distributed control surfaces.

To measure the design efficiency, the optimised composite wing with trailing-edge flaps (iv) is benchmarked against an all-metallic wing obtained with the same methodology (iii). The passively tailored study cases (i) and (ii) are used as reference designs for the adaptive study cases (iii) and (iv). Performance is evaluated based on the total fuel burned and a payload-range efficiency parameter. Apart from fuel burn comparisons, special attention is drawn into investigating the interdependencies between control surface scheduling design variables and laminate stiffnesses through aerostructural load re-distribution, which, in turn, relieves the manoeuvre loads and minimises drag.

https://doi.org/10.1017/aer.2018.66 Published online by Cambridge University Press

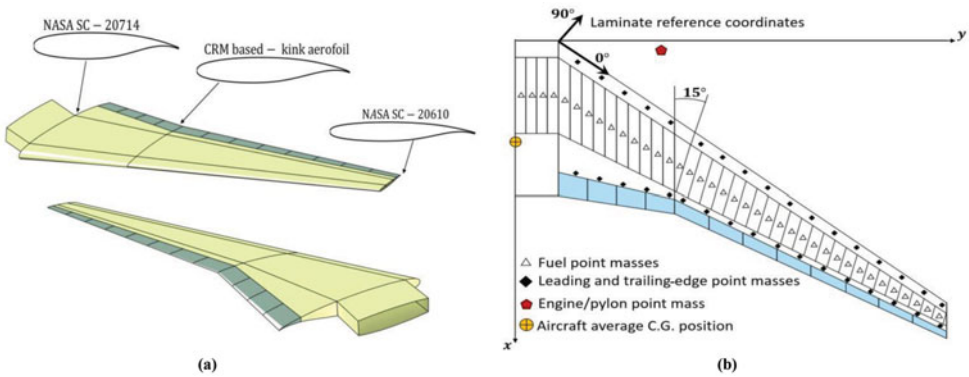


Figure 1. (Colour online) Wing aerodynamic and structural layouts. (a) Aerodynamic shape of the reference wing model. (b) Wingbox structural configuration.

The paper is structured as follows. First, we describe the reference aircraft geometry and finite element aeroelastic model in Section 2. The aeroelastic solver used for load and stress evaluations, and additional aircraft drag considerations are briefly discussed in Section 3. Next, laminate constitutive equations and manufacturing constraints are formulated in Section 4. The optimisation problem statement is introduced formally in Section 5, with detailed descriptions of the optimisation algorithm, design variables and design constraints used. Finally, the results in terms of structural characteristics variations, spanwise loads, control surface deflections and first-order performance metrics are assessed and discussed in Section 6, followed by concluding remarks drawn in Section 7.

2.0 BASELINE LAYOUT AND GENERAL DESCRIPTION

The aircraft model used throughout this work is based on open research data provided in the development of the NASA Common Research Model (CRM)[29]. The wing configuration is demonstrative of the state-of the-art of a contemporary long-range airliner (operating in the 300-seat market category) designed for nominal cruise flights at transonic speeds, more specifically, at Mach number $M = 0.85$ with a design lift coefficient of $C_L = 0.50$.

The wing planform spans 58.7 m, with an aspect ratio 9 and a quarter-chord sweep angle of 35°. The trailing-edge kinks at approximately 37% of the semi-span. The mean aerodynamic chord and the taper ratio are 7.00 m and 0.275, respectively. The wing root employs a NASA SC-20714 supercritical aerofoil with a maximum thickness of 14% and with 7% of maximum camber. For the outboard wing section, a NASA SC-20610 aerofoil is used. A lofted version of the CRM aerofoil developed for the 65% span station is utilised at the wing Yehudi break (kink) resulting in a maximum thickness of 12.3% with 6.3% of maximum camber. A total of 12 discrete trailing-edge controls, distributed along the wingspan as indicated in Fig. 1, are utilised as a mechanism for improved aerostructural performance. These devices occupy approximately 15% of the local wing chord.

The wingbox follows a conventional structural architecture, which is built around two main full-depth straight spars (i.e. front and rear spars) with in-between ribs and stiffened skins. The front and rear spars lie respectively at 11% and 60% of the wing root chord, and taper linearly towards the wing outboard section to correspondingly 30% and 65% of the

https://doi.org/10.1017/aer.2018.66 Published online by Cambridge University Press

Table 1
Composite and metallic material properties

Aluminium material		Composite material			
Property	**Value**	**Property**	**Value**	**Property**	**Value**
E	71.7 GPa	E_{11}	128 GPa	G_{23}	4.5 GPa
ν	0.33	E_{22}	11 GPa	ρ	1,520 kg/m³
σ_Y	420 MPa	ν_{12}	0.28	S_{12}	78 MPa
ρ	2,780 kg/m³	G_{12}	4.5 GPa	t	0.125 mm
Strain allowable: 5,500 μm		strain allowable in tension: 3,500 μm		strain allowable in compression: 3,500 μm	

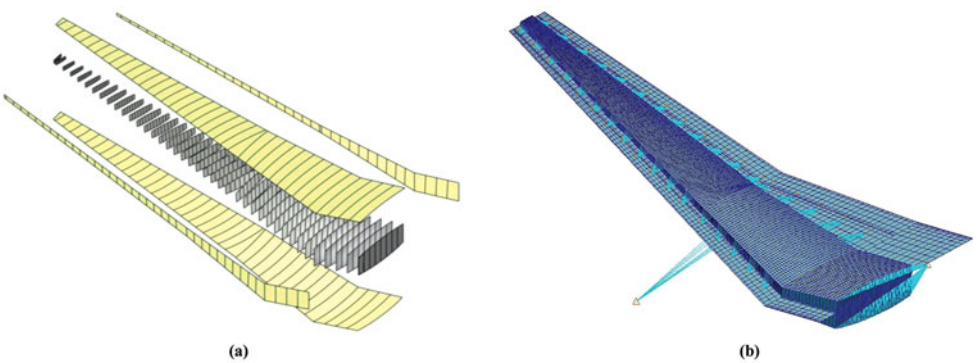


Figure 2. (Colour online) Wingbox model. (a) Wingbox designable patches for spars, ribs and skins. (b) Wing structural FE model and aerodynamic panelling.

local chord. The box structure comprises three main wing partitions: wing fuselage junction (0-10%), inner wing (10-37%), and outer wing (37-100%). A total of 40 ribs is used, uniformly distributed piecewise within each of the three wing partitions. The first 15 ribs are aligned with the free stream, whereas the remaining (in the outer wing) are approximately perpendicular to the leading-edge spar. Each skin panel is stiffened with seven L-shaped running-through stringers, equally spaced across the local chord and parallel to the wing local sweep angle. Figure 1(a) and (b) portray the wing aerodynamic shape and a general layout of the wingbox structural configuration. The material properties used in the study are listed in Table 1. The laminate's reference frame for both upper and lower skins is defined according to Fig. 2(a) with 0° ply fibre direction aligned with the wing leading edge.

The wingbox model is auto-meshed with in-house MATLAB and MSC/PATRAN scripts using shell elements for the skins, ribs and spars (for improved laminate principal stresses and strains calculations), and beam elements for the stiffeners. To emulate aircraft weight due to non-structural components, lumped masses connected to the spars via rigid body connectors with distributed loadings are employed for the fuel load, engine/nacelle set and leading and trailing-edge sub-structures. An additional balance lumped mass is placed at the aircraft centre of gravity (C.G.) to characterise fuselage, payload, and reserve fuel contributions to the aircraft

https://doi.org/10.1017/aer.2018.66 Published online by Cambridge University Press

overall inertia. The lumped masses for trailing-edge devices are placed approximately at the control hinge line.

The model is limited to a Maximum Take-Off Weight (MTOW) of approximately 255,000 kg, with an Operational Empty Weight (OEW) of 137,900 kg, 95,500 kg of which are due to the fuselage and tail assemblies, 7,500 kg to each engine/nacelle and approximately 10,000 kg to the half-wing structure. A total of 1,200 kg are used as non-structural mass for the leading-edge devices and 2,500 kg for the trailing-edge controls and actuators (the actuator masses are assumed to be proportional to the flap area).

To allow for detailed variations in both material properties and thicknesses during the optimisation process, the structural Finite Element (FE) model is divided into various tailorable-zones, as shown in Fig. 2(a). Each wing skin features a total of 39 rib-bay patches. Similarly, 39 designable patches are used for each spar.

The aerodynamic panelling is divided into two lifting surfaces: a main wing and a tailplane used for static longitudinal trim calculations. The aerodynamic mesh consists of a total of 2,105 boxes evenly distributed in the spanwise direction. For the chordwise topology, a cosine distribution is used to accurately capture pressure variations at the wing leading and trailing-edges (see Fig. 2(b)). The wing jig-twist and aerofoil camber distributions are input via Direct Matrix Input (DMI) entries as a W2GJ NASTRAN matrix by changing the effective downwash angle of each aerodynamic element.

3.0 AEROELASTIC ANALYSIS AND STRUCTURAL STABILITY CALCULATIONS

In this work, NASTRAN routine 144 is used to perform longitudinal trim analyses and to compute static aeroelastic loads and aerostructural design metrics. NASTRAN implements the Doublet-Lattice subsonic lifting surface theory (DLM), which can estimate rigid and flexible aerodynamic loads. The choice of the aerodynamic solver is based on a trade-off between computational cost and accuracy of the solution. Advanced CFD techniques are known to capture important transonic effects better, such as the drag rise behaviour and shocks formation, though a substantial increase in computational cost is expected. Here, we use a much simpler, but faster, aerodynamic solver. Since the DLM is based on a linearised aerodynamic potential theory, the abovementioned transonic effects are all neglected, which reduces the accuracy of the predicted drag and aerodynamic loads. Consequently, care must be taken in interpreting the solutions found, as these are only acceptable as first-order estimates.

A total of five representative symmetric load cases (limited by computational resources) are considered in the optimisation problem as summarised in Table 2. The first two load cases are mainly for sizing purposes: a 2.5 g pull-up and a -1.0 g push-down manoeuvres at mid-cruise altitude and speed with maximum take-off weight. The last three load cases are used for fuel burn minimisation trade-off studies. The overall cruise profile assumes the shape of a "cruise-climb" mission (see Fig. 3) with increasing altitude for a constant Mach number as fuel is consumed. An aircraft payload (30,000 kg) and mission range (5,000 nmi) were chosen based on Ref. (15).

The wingbox structural stability is evaluated via a linear buckling analysis (as implemented in NASTRAN solution 105) using the aerodynamic loads of the M1 and M2 load cases. The first five buckling load factors are evaluated and used as a design constraint as explained in Section 5.2.2.

https://doi.org/10.1017/aer.2018.66 Published online by Cambridge University Press

Table 2
Static aeroelastic load cases considered

Load case	Load factor	Altitude (ft)	Fuel (kg)	Mach	Payload (kg)	Range (nmi)
Manoeuvre 1 (M1)	2.5	35,000	86,500 (max)	0.85	30,000	–
Manoeuvre 2 (M2)	–1.0	35,000	86,500 (max)	0.85	30,000	–
Cruise 1 (C1)	1.0	33,000	73,525 (85%)	0.85	30,000	1,667
Cruise 2 (C2)	1.0	35,000	43,250 (50%)	0.85	30,000	1,667
Cruise 3 (C3)	1.0	37,000	12,974 (15%)	0.85	30,000	1,667

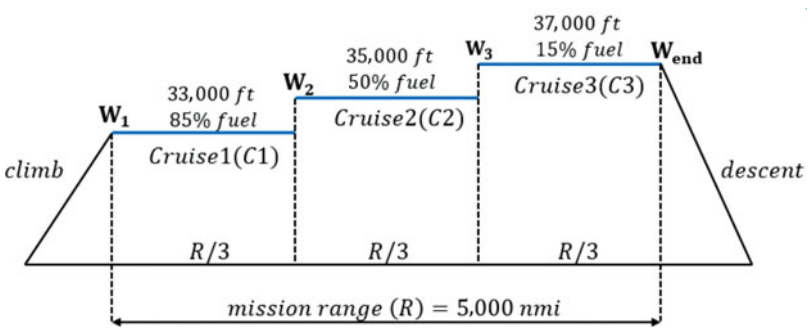


Figure 3. (Colour online) Cruising flight mission profile divided into three phases.

3.1 Total drag dissipation estimate

For fuel burn calculations, an accurate and realistic estimation of the drag build-up for cruising flights is essential, because this can significantly influence the optimisation final solution. To address this issue, we account for profile drag and wave drag contributions as presented in Ref. (11). With this approach, wing profile and wave drag coefficients (C_{D_p} and C_{D_c}, respectively), which are otherwise not included in standard DLM, are estimated semi-empirically. This approach is used here as a first-order approximation of the aircraft wing drag. The lift-induced drag (C_{D_i}) is estimated with a Trefftz-plane method as proposed in Ref. (30). The profile drag is calculated as a quadratic function of the local lift coefficient (c_l), so that

$$C_{D_p} = C_{D_0}\left[1 + \frac{0.38}{\cos\Lambda_{le}}\left(c_l^2\right)\right], \qquad \ldots(1)$$

where Λ_{le} is the wing leading-edge sweep angle. Differently from Ref. [11], here, the C_{D_0} coefficient used to estimate the profile drag, is calculated according to Ref. [37] as described next. This coefficient is related to zero-lift drag dissipations of viscous skin-friction nature,

https://doi.org/10.1017/aer.2018.66 Published online by Cambridge University Press

usually associated with flow separations or other similar flow instabilities. Its contribution to the total aircraft drag is proportional to viscous drag coefficient (C_f), form factor $(\mathcal{F})$ and wing wetted area ratio (S_{wetted}/S), so that

$$C_{D_0} = C_f \mathcal{F} \frac{S_{\text{wetted}}}{S}, \quad \ldots (2)$$

where S is the wing planform area. In Equation (2), the viscous drag coefficient is calculated assuming a flat plate theory for turbulent flows and is given by

$$C_f = \frac{0.455}{(\log Re_x)^{2.58}\left(1 + 0.144M^2\right)^{0.65}}. \quad \ldots (3)$$

In Equation (3), M is the free-stream Mach number and Re_x is the wing average Reynolds number estimated using the mean aerodynamic chord $(\bar{c})$, the component of the free-stream velocity (U_0) and the kinematic viscosity (ν)

$$Re_x = \bar{c} U_0 \cos \Lambda_{le} / \nu. \quad \ldots (4)$$

The form factor $\mathcal{F}$ accounts for the rise in wing skin-friction drag due to flow separations and is described as a function of the wing maximum thickness position $(x/c)_{\max}$, the thickness-to-chord ratio (t/c) spanwise variation and the geometric sweep angle of the maximum thickness line $(\Lambda_{t/c_{\max}})$. It can be calculated according to the relationship

$$\mathcal{F} = \left[1 + \frac{0.6}{(x/c)_{\max}}\left(\frac{t}{c}\right) + 100\left(\frac{t}{c}\right)^4\right]\left[1.34M^{0.18}\left(\cos\left(\Lambda_{t/c_{\max}}\right)\right)^{0.28}\right]. \quad \ldots (5)$$

The total aircraft drag coefficient results from the contributions of the profile drag, wave drag, lift-induced drag and additional losses $(C_{D_{\text{losses}}})$ due to non-modelled fuselage, vertical tail and other drag sources (a value of 100 drag counts is assumed for the $C_{D_{\text{losses}}}$ contribution) such that

$$C_D = C_{D_p} + C_{D_c} + C_{D_l} + C_{D_{\text{losses}}}. \quad \ldots (6)$$

4.0 FUNDAMENTAL LAMINATE CONSTITUTIVE EQUATIONS

According to Classical Laminated Plate Theory (CLPT)[38], a plate's two-dimensional displacement field, described in terms of its mid-plane strains and curvatures, can be related to resultant loads (generalised forces and moments) by the extensional (in-plane), **A**,

https://doi.org/10.1017/aer.2018.66 Published online by Cambridge University Press

bending-extension coupling, **B**, and bending (out-of-plane), **D**, stiffness matrices and is represented in compact form as

$$\begin{bmatrix} \mathbf{N} \\ \mathbf{M} \end{bmatrix} = \begin{bmatrix} \mathbf{A} & \mathbf{B} \\ \mathbf{B} & \mathbf{D} \end{bmatrix} \begin{bmatrix} \boldsymbol{\varepsilon}^{\mathbf{0}} \\ \boldsymbol{\kappa} \end{bmatrix}. \quad \ldots (7)$$

Equation (7) can be written more explicitly in terms of generalised forces, $\mathbf{N} = \{N_x, N_y, N_{xy}\}^T$; and moments, $\mathbf{M} = \{M_x, M_y, M_{xy}\}^T$; and related strains, $\boldsymbol{\varepsilon}^{\mathbf{0}} = \{\varepsilon_x^o, \varepsilon_y^o, \gamma_{xy}^o\}^T$; and curvatures, $\boldsymbol{\kappa} = \{\kappa_x, \kappa_y, \kappa_{xy}\}^T$, such that

$$\begin{Bmatrix} N_x \\ N_y \\ N_{xy} \\ M_x \\ M_y \\ M_{xy} \end{Bmatrix} = \begin{bmatrix} A_{11} & A_{12} & A_{16} & B_{11} & B_{12} & B_{16} \\ & A_{22} & A_{26} & & B_{22} & B_{26} \\ sym & & A_{66} & sym & & B_{66} \\ B_{11} & B_{12} & B_{16} & D_{11} & D_{12} & D_{16} \\ & B_{22} & B_{26} & & D_{22} & D_{26} \\ sym & & B_{66} & sym & & D_{66} \end{bmatrix} \begin{Bmatrix} \varepsilon_x^o \\ \varepsilon_y^o \\ \gamma_{xy}^o \\ \kappa_x \\ \kappa_y \\ \kappa_{xy} \end{Bmatrix}, \quad \ldots (8)$$

where **N** and **M** are obtained by integrating stresses through the laminate thickness and A_{ij}, B_{ij}, and D_{ij}, with $i, \ j = 1, 2, 6$, are functions of material properties and stacking sequence.

Examination of Equation (8) shows insight on the type of coupling produced by a laminate and the significance of stiffness matrices as a means of passive aeroelastic tailoring. Shear-extension coupling may occur due to the presence of A_{16} and A_{26}, which relate in-plane normal forces with shear deformation and shear forces with in-plane elongations. Similarly, extension-extension coupling can be achieved with A_{12}, which relates normal forces with normal elongations in the principal directions. In balanced laminates (i.e. for every ply at an angle θ, there must be a ply with orientation $-\theta$ within the stacking sequence) the elements $A_{16} = A_{26} = 0$, and thus, shear-extension coupling is not possible.

The out-of-plane elements D_{16} and D_{26} measure the bend-twist coupling, which causes applied bending moments to twist the laminate, and resultant twist moments to produce out-of-plane curvatures. Finally, the out-of-plane stiffness D_{12} produces bending-bending coupling, causing resultant moments to induce curvatures in the direction perpendicular to the applied load. In this work, couplings induced by bending-extension stiffness coefficients are not considered for reasons discussed in Section 4.1.

In aerostructural optimisation problems, wingbox structures are commonly subdivided into a number of tailorable-zones encompassing rib and/or stringer-bay patches. A complete detailed parameterisation of composite structures at the stacking sequence level often results in an impractical number of design variables, which may bring about computational limitations. Tsai et al.[39] and Tsai and Hahn[40] introduced an alternative formulation for the **A**, **B, D** matrices that is beneficial for optimisation purposes because it reduces the total number of design variables significantly. Additionally, its continuous nature makes it suitable for gradient-based optimisers. The in-plane and out-of-plane stiffnesses can then be expressed as linear functions of five material invariants (which can be calculated from the material properties presented in Table 1), U_k, and eight (twelve when $B \neq 0$) lamination parameters,

https://doi.org/10.1017/aer.2018.66 Published online by Cambridge University Press

ξ_i^j, with $i = 1, \ldots 4$, $j = A, D$, and $k = 1, \ldots 5$, such that

$$\begin{Bmatrix} A_{11} \\ A_{22} \\ A_{12} \\ A_{66} \\ A_{16} \\ A_{26} \end{Bmatrix} = h \begin{bmatrix} 1 & \xi_1^A & \xi_3^A & 0 & 0 \\ 1 & -\xi_1^A & \xi_3^A & 0 & 0 \\ 0 & 0 & -\xi_3^A & 1 & 0 \\ 0 & 0 & -\xi_3^A & 0 & 1 \\ 0 & \xi_2^A/2 & \xi_4^A & 0 & 0 \\ 0 & \xi_2^A/2 & -\xi_4^A & 0 & 0 \end{bmatrix} \begin{Bmatrix} U_1 \\ U_2 \\ U_3 \\ U_4 \\ U_5 \end{Bmatrix}, \quad \ldots (9)$$

$$\begin{Bmatrix} D_{11} \\ D_{22} \\ D_{12} \\ D_{66} \\ D_{16} \\ D_{26} \end{Bmatrix} = \frac{h^3}{12} \begin{bmatrix} 1 & \xi_1^D & \xi_3^D & 0 & 0 \\ 1 & -\xi_1^D & \xi_3^D & 0 & 0 \\ 0 & 0 & -\xi_3^D & 1 & 0 \\ 0 & 0 & -\xi_3^D & 0 & 1 \\ 0 & \xi_2^D/2 & \xi_4^D & 0 & 0 \\ 0 & \xi_2^D/2 & -\xi_4^D & 0 & 0 \end{bmatrix} \begin{Bmatrix} U_1 \\ U_2 \\ U_3 \\ U_4 \\ U_5 \end{Bmatrix}, \quad \ldots (10)$$

where h is the laminate thickness and

$$\xi_{[1,2,3,4]}^A = \frac{1}{h} \int_{-h/2}^{h/2} [\cos 2\theta, \sin 2\theta, \cos 4\theta, \sin 4\theta]\, dz, \quad \ldots (11)$$

$$\xi_{[1,2,3,4]}^D = \frac{12}{h^3} \int_{-h/2}^{h/2} [\cos 2\theta, \sin 2\theta, \cos 4\theta, \sin 4\theta]\, z^2 dz, \quad \ldots (12)$$

with $\theta(z)$ corresponding to the ply angle along the through-thickness coordinate z.

4.1 Laminate design guidelines

Over the last decades, the search for more structurally efficient materials, combined with a number of lessons learned within the aerospace industry, resulted in the development of a series of composite design guidelines. These guidelines may differ from organisation to organisation but serve the purpose of offering sufficient confidence to the design of manufacturable composite airframes. Moreover, these guidelines are a means to provide design solutions (or restrictions) that satisfy certification purposes and production requirements linked to manufacturing limitations.

Reference (41) provides a more comprehensive discussion about the development and justification of these "rules of thumb". The most common design guidelines are implemented in this work.

(a) Only unidirectional plies restricted to four main directions (i.e. 0°, ±45°, and 90°) are allowed in the laminate stacking sequence.

(b) Laminates must have a minimum of 10% of their plies oriented in each one of the four principal directions.

(c) A maximum of 60% of plies oriented in any direction is allowed in the laminate.

(d) At least one pair of ±45° plies should be placed in the laminate outer plies.

(e) The laminate must be balanced ($A_{16} = 0$ and $A_{26} = 0$) to eliminate shear-extension coupling, i.e. the number of −45° and +45° plies must be the same.

https://doi.org/10.1017/aer.2018.66 Published online by Cambridge University Press

(f) Laminate sequences must be symmetric about their middle surface in order to remove bending-extension coupling ($B_{ij} = 0$).

(g) A maximum of four plies of the same orientation and thickness can be stacked together. This is to prevent matrix-cracking between layers.

(h) All layers of the thinner laminate must be present in all other wing skin panels. In other words, the laminate must share layers between adjacent panels in order to fulfil blending constraints.

Note that, in particular, design guideline (e) limits considerably the tailoring capability of the composite skins by eliminating shear-extension coupling. For this reason, the laminate configuration adopted here can be unbalanced ($A_{16} \neq 0$ and $A_{26} \neq 0$).

4.2 Criteria for lamination parameters feasibility

As defined by Equations (11) and (12), lamination parameters are continuous variables of trigonometric characterisation, and therefore, they must be constrained to mathematically feasible regions that are enclosed by the relationships suggested in Refs (42,43). These are

$$\begin{gathered} 2\left(1+\xi_3^i\right)\left(\xi_2^i\right)^2 - 4\xi_1^i\xi_2^i\xi_4^i + \left(\xi_4^i\right)^2 \leq \left(\xi_3^i - 2\left(\xi_1^i\right)^2 + 1\right)\left(1-\xi_3^i\right), \\ \left(\xi_1^i\right)^2 + \left(\xi_2^i\right)^2 \leq 1, \\ \left(\xi_j^A - 1\right)^4 - 4\left(\xi_j^A - 1\right)\left(\xi_j^D - 1\right) \leq 0, \\ \left(\xi_j^A + 1\right)^4 - 4\left(\xi_j^A + 1\right)\left(\xi_j^D + 1\right) \leq 0, \\ -1 \leq \xi_j^i \leq 1, \end{gathered} \quad \ldots (13)$$

where $i = A,\ D$ and $j = 1, \ldots, 4$. These inequalities are employed in the optimisation problem as nonlinear constraints in order to ensure retrieval of feasible stacking sequences.

In order to comply with the manufacturing guidelines (b) and (c) of Section 4.1, additional relations adapted from Ref. 44 are implemented as design constraints at lamination parameter level so that

$$\begin{aligned} &0^\circ \text{ ply } \%: \quad 0.1 \leq \left(\xi_3^A + 2\xi_1^A + 1\right)/4 \leq 0.6, \\ &90^\circ \text{ ply } \%: \quad 0.1 \leq \left(\xi_3^A - 2\xi_1^A + 1\right)/4 \leq 0.6, \\ &+45^\circ \text{ ply } \%: \quad 0.1 \leq \left(1 + 2\xi_2^A - \xi_3^A\right)/4 \leq 0.6, \\ &-45^\circ \text{ ply } \%: \quad 0.1 \leq \left(1 - 2\xi_2^A - \xi_3^A\right)/4 \leq 0.6. \end{aligned} \quad \ldots (14)$$

5.0 OPTIMISATION PROBLEM DESCRIPTION

In this section, we investigate the synergies and trade-offs between passive aeroelastic tailoring and adaptive aeroelastic deformation of a representative composite wing for fuel burn minimisation by optimising laminate thickness and stiffness distributions, jig-twist shape and controls deflections through different segments of a nominal cruise mission and critical symmetric manoeuvres.

A total of four design studies, labelled "OPT" 1 to 4, are performed. The first and second design studies tailor the wingbox structure for passive adaptation (controls are held fixed with zero deflection) for two different wing configurations, i.e. a metallic and a hybrid wing with composite skins, respectively. The aforementioned exercise is repeated in OPT 3 and OPT 4

https://doi.org/10.1017/aer.2018.66 Published online by Cambridge University Press

Table 3
Optimisation study cases

Optimisation study	Type of structure	Load alleviation and minimum drag mechanisms
OPT1	All-metallic wing	Passive aeroelastic tailoring
OPT2	Composite skins	
OPT3	All-metallic wing	Aeroservoelastic tailoring (controls employed)
OPT4	Composite skins	

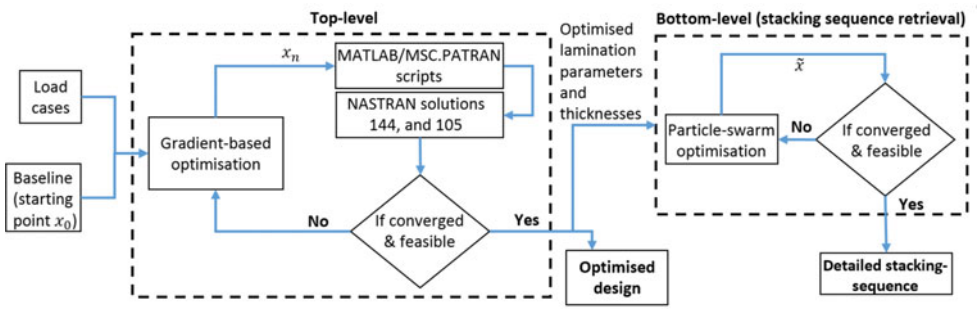


Figure 4. (Colour online) Bi-level optimisation workflow.

with the trailing-edge controls employed as a mechanism for adaptive load alleviation for a 2.5 g pull-up manoeuvre and to minimise the overall drag for cruise (load cases as described in Section 3). These optimisation studies are summarised in Table 3.

The laminate ply-book (detailed ply orientations and stacking sequence) of the composite designs are retrieved via a separate optimisation level. Since the conversion from lamination parameter space to stacking sequence space may entail some stiffness discrepancies, the aerostructural performance of the designs defined with detailed ply-books is then assessed and benchmarked by comparing it against OPT 1 to 4.

5.1 Optimisation workflow

The optimisation workflow implemented in this work is represented in Fig. 4. The optimisation process is divided in two separate and consecutive levels (there is no feedback response between the first and second level), distinguished as "top-level" and "bottom-level" optimisations.

The top-level optimisation starts with the baseline design (x_0) and the load cases described in Sections 2 and 3 as input and uses a gradient-based optimiser to calculate aeroelastic sensitivities of the objective function and design constraints, with respect to the design variables. At this level, a series of in-house MSC/PATRAN and MATLAB scripts are used to generate input files for the aeroelastic calculations (NASTRAN routines 144 and 105). The optimisation continues until it reaches one of the stopping criteria (i.e. thresholds for the optimisation step-size and first-order optimality measure).

Based on the lamination parameters and thicknesses from the top-level optimisation, the bottom-level optimisation uses a particle-swarm algorithm to retrieve feasible stacking

https://doi.org/10.1017/aer.2018.66 Published online by Cambridge University Press

sequences and detailed wing skin ply-books with blending considerations. Both optimisation levels are described in more detail in the following sections.

5.2 Top-level optimisation using a gradient-based algorithm

The top-level optimisation problem is solved using MATLAB's gradient-based algorithm *fmincon*. Gradients of the objective function and design constraints with respect to the design variables are calculated via forward finite differences with a Sequential Quadratic Programming (SQP) approach[45].

Matlab's implementation of the SQP method is purposely designed for nonlinearly constrained optimisation problems being efficient in terms of memory usage and execution time. When the constraints are not satisfied, the SQP solver uses the penalty function approach that combines the objective and constraint functions into a single merit function, which is then minimised with relaxed bounds. This approach results in a better understanding of the conflicting trade-offs that governs the optimisation problem, usually resulting in a superior solution when compared to other gradient-based approaches. The Hessian of the Lagrangian is updated at every iteration using a quasi-Newton method to resolve a quadratic programming sub-problem in order to determine the line search direction.

The next sections present the design variables and design constraints parameterisation in detail as well as the objective function adopted for the bi-level optimisation.

5.2.1 Design variables parameterisation

The top-level optimisation uses four different sets of continuous design variables divided into: (1) thicknesses of the main wing sub-structure components (x_t), i.e. spars and skins; (2) in-plane and out-of-plane lamination parameters (x_{comp}) for the composite skins of OPT 2 and OPT 4; (3) geometric variables (x_{jig}) which define the wing jig-twist shape; and (4) trailing-edge control deflections (x_{ctrl}) for each load case considered in the analysis.

For all design variables, a Piecewise Cubic Hermite Interpolating Polynomial (PCHIP) technique is used to describe multiple design properties variations in the spanwise direction, i.e. one PCHIP for thickness of each spar and each skin, lamination parameters $\xi^{A,D}_{[1,2,3]}$ of each skin, jig-twist and trailing-edge control rotations of each load case. This technique fits a piecewise polynomial passing through a fixed number of equally spaced control points placed from wing root to wingtip. For thicknesses and lamination parameters, the PCHIP is interpolated over 39 designable patches (as shown in Fig. 2(a)); jig-twist variables are interpolated at 84 aerodynamic strips and four structural sections (root, tip and spar breaks), whereas control surface rotations are interpolated at twelve discrete control surfaces.

Using the PCHIP technique to describe variations in properties along the wing structure significantly reduces the number of design variables, which is convenient for the optimisation algorithm chosen, because the computational cost of each iteration is proportional to $n + 1$ function evaluations, where n is the total number of design variables. Nonetheless, the quality of the final solution is strongly affected by the number and location of the control points.

It is found that six control points for thicknesses and lamination parameters (from which only the first five are used as design variables) and five control points for the remaining design variables offers a good trade-off between computational cost and optimality of the solutions. Note that, for thicknesses and lamination parameters, the sixth control point, placed at the wingtip, is fixed at 3 mm and zero, respectively – initial studies showed no sensible variation in the objective function if this control point was used as a design variable. Furthermore, this special type of piecewise parameterisation guarantees continuity and smoothness of structural

https://doi.org/10.1017/aer.2018.66 Published online by Cambridge University Press

Table 4
Set of design variables used in the top-level optimisation

Design variables type			OPT 1	OPT 2	OPT 3	OPT 4
Thickness (x_t)	Spars		5 (×2)	5 (×2)	5 (×2)	5 (×2)
	Skins		5 (×2)	5 (×2)	5 (×2)	5 (×2)
Lamination parameters (x_{comp})	Extensional (in-plane), **A**	ξ_1^A	0	5 (×2)	0	5 (×2)
		ξ_2^A	0	5 (×2)	0	5 (×2)
		ξ_3^A	0	5 (×2)	0	5 (×2)
	Bending (out-of-plane), **D**	ξ_1^D	0	5 (×2)	0	5 (×2)
		ξ_2^D	0	5 (×2)	0	5 (×2)
		ξ_3^D	0	5 (×2)	0	5 (×2)
geometric (x_{jig})	Wing jig-twist		5	5	5	5
Control scheduling (x_{ctrl})	Trailing-edge deflections (five variables per load case)		0	0	5 (×5)	5 (×5)
Total number of design variables:			25	85	50	110

properties along the wing, which, presumably, favours the design of blended composite wing skins.

For all of the optimisation study cases considered here, the design variables defining the thickness distribution are allowed to range from 3 mm and 30 mm. In-plane and out-of-plane lamination parameters are bounded by the feasibility relationships of Equations (13) and (14) discussed in Section 4.2. Jig-twist variables can vary from 4° to −1° whilst control surface deflections range from –8° to 8°. The design variables are standardised and nondimensionalised to vary between −1 and 1 to assure a good convergence rate and to avoid insensitiveness to step-size variations of one or more of the variables, because their absolute order of magnitude may differ widely otherwise. Table 4 summarises the number and type of design variables used in the optimisation problems.

5.2.2 *Design constraints*

In order to restrict the design to feasible and physically meaningful solutions, we use a number of design constraints in the top-level optimisation analysis. To comply with the limitations of the aeroelastic solver chosen, the first set of design constraints narrows the wing structural deformations to the linear elastic behaviour only. This is done by defining two main deformation constraints: (a) a maximum twist angle and (b) a maximum bending deflection. These constraints are written as

$$C_{\text{twist}} = \frac{\theta_{\text{tip}}}{\theta_{\text{allowed}}} \leq 1, \qquad \ldots (15)$$

$$C_{\text{bending}} = \frac{z_{\text{tip}}}{z_{\text{allowed}}} \leq 1, \qquad \ldots (16)$$

https://doi.org/10.1017/aer.2018.66 Published online by Cambridge University Press

where $z_{allowed}$ is the maximum allowed wingtip vertical displacement (limited to 15% of the semi-span) and $\theta_{allowed}$ is the maximum permissible twist deformation, which is set to 10°.

Buckling load factors, composite principal stresses and strains, and Mises-based stresses and strains for metallic parts are constrained with the Kreisselmer-Steinhauser (KS) aggregation technique[46,47]. The aggregation formula used to constrain principal stresses and strains is given by

$$KS_{\text{metric}} = C_{\max} + \frac{1}{\rho_{KS}} \ln \left[\sum_{i=1}^{n} e^{\rho_{KS}(C_i - C_{\max})} \right], \quad \ldots (17)$$

where C_i is the ratio between the constraint metric for the i^{th} finite element and its allowed value (yield stress or maximum strain) and $C_{\max}$ is the maximum constraint metric in the current design point. The parameter ρ_{KS} represents the aggregation factor which is set to 50. A KS constraint is said to be violated when its value is greater than one. For each aeroelastic load case, Equation (17) is used to aggregate (a) major and minor principal stresses and strains for the laminated wing skins, and (b) equivalent von Mises stresses and strains for the metallic sub-structures. For buckling load factors, the first five eigenvalues of the most critical load cases are aggregated with a modified KS formula as proposed in Ref. 21.

$$KS_{\text{Buckling}} = 2 - \lambda_{\min} + \frac{1}{\rho_{KS}} \ln \left[\sum_{i=1}^{n} e^{\rho_{KS}(\lambda_{\min} - \lambda_i)} \right], \quad \ldots (18)$$

where $\lambda_{\min}$ is the minimum buckling load factor. This technique is beneficial for optimisation purposes because it simplifies and reduces total number of design constraints considerably (usually at the finite element level), combining them into a single parameter per constrained design metric. It may also improve robustness against the switching of critical buckling modes at reduced computational cost[21].

The use of trailing-edge controls can alter the resulting trim Angle-of-Attack (AoA) to values lower than those acceptable for passenger comfort (i.e. slightly negative AoA). For this reason, the trim AoA for all cruise flight conditions is constrained to a minimum of 1.5°. Table 5 summarises the number and type of design constraints used in the optimisation problems. Note that lamination parameters feasibility relationships are applied at each control point, whereas KS constraints are used for each load case considered (except for KS_{Buckling}, where only the buckling loads of the M1 and M2 manoeuvres are of interest).

5.2.3 Objective function

The objective function used in the top-level optimisation is to minimise the total fuel burned during cruise. For a particular mission range, the fuel consumed can be estimated using the well-known Breguet range equation assuming that the Thrust Specific Fuel Consumption ($TSFC$), the aircraft speed (U_0) and the lift efficiency (C_L/C_D) remain constant along a given cruise segment. Under these assumptions, the range equation is

$$R = \frac{U_0}{TSFC} \left(\frac{C_L}{C_D} \right) \ln \left(\frac{W_{\text{begin}}}{W_{\text{end}}} \right), \quad \ldots (19)$$

where the $TSFC$ is taken as a function of the altitude, decreasing 1% for every increment of 2,500 ft in the flight level (as a reference, a value of 0.53 lb/(lbf·h) is adopted for 35,000 ft).

https://doi.org/10.1017/aer.2018.66 Published online by Cambridge University Press

Table 5
Set of design constraints used in the top-level optimisation

Inequality design constraints			OPT 1 & 3	OPT 2 & 4
Elastic structural deformations (one per load case)	Maximum twist	C^i_{twist}	5	5
	Maximum bending	C^i_{bending}	5	5
Trim angle-of-attack		C^i_{AoA}	3	3
Structural constraints (one per load case)	Principal strains	$KS^i_{\text{MinStrain}}$	0	5
		$KS^i_{\text{MaxStrain}}$	0	5
	Principal stresses	$KS^i_{\text{MinStress}}$	0	5
		$KS^i_{\text{MaxStress}}$	0	5
	von Mises strains	$KS^i_{\text{Strain-Mises}}$	5×2 (skins and spars)	5
	von Mises stresses	$KS^i_{\text{Stress-Mises}}$	5×2 (skins and spars)	5
	Buckling load factors	KS_{Buckling}	2	2
Lamination parameters feasibility region	Given by Equations (12) and (13)	$C^{\text{Upper skin}}_{\text{Lam}}$	0	100
		$C^{\text{Lower skin}}_{\text{Lam}}$	0	100
Total number of constraints:			35	245

Equation (19) can be rearranged in terms of fuel burned for given cruise segment (FB_i) and written as

$$FB_i = W_i - W_{i+1} = W_i[1 - \exp(-RS_i)], \quad \ldots(20)$$

where W_i and W_{i+1} are the initial and final aircraft weight of the i^{th} cruise flight segment, respectively, and the parameter RS_i is

$$RS_i = \frac{R_i TSFC_i}{U_0(C_L/C_D)_i}. \quad \ldots(21)$$

From Equations (20) and (21), it can be shown that the total fuel consumed over the entirety of the cruise-climb mission (for n cruise segments) is a function of the initial cruise weight

https://doi.org/10.1017/aer.2018.66 Published online by Cambridge University Press

(W_1) and the summation of RS_i parameters, as in

$$FB_{\text{total}} = W_1 \left[1 - \exp\left(- \sum_{i=1}^{n} RS_i \right) \right]. \quad \ldots (22)$$

The objective function is obtained from Equation (22) by normalising to the order of unity using a reference baseline value

$$f_{\text{obj}}^{\text{top-level}}(\mathbf{x}) = FB_{\text{total}} / FB_{\text{baseline}}, \quad \ldots (23)$$

In conclusion, the top-level optimisation problem can be formulated as

$$\underset{\mathbf{x} \in \Omega}{\text{minimise}}\, f_{\text{obj}}^{\text{top-level}}(\mathbf{x})$$

$$\text{with respect to} : \mathbf{x} = \left\{ x_{\text{t}}, x_{\text{comp}}, x_{\text{jig}}, x_{\text{crtl}} \right\}^T \text{ and } \Omega = \{ \mathbf{x} | C(\mathbf{x}) \leq 0 \}$$

$$\text{such that } C(\mathbf{x}) = \begin{cases} KS^i_{\text{MinStrain}} - 1; \\ KS^i_{\text{MaxStrain}} - 1; \\ KS^i_{\text{MinStress}} - 1; \\ KS^i_{\text{MaxStress}} - 1; \\ KS^i_{\text{Stress-Mises}} - 1; \\ KS^i_{\text{Strain-Mises}} - 1; \\ KS^{i=1,2}_{\text{Buckling}} - 1; \\ C^i_{\text{AoA}} - 1; \\ C^i_{\text{twist}} - 1; \\ C^i_{\text{bending}} - 1; \\ C^i_{\text{bending}} \\ -1 \leq \mathbf{x} \leq 1 \end{cases} \quad i = 1, \ldots, N_L, \quad \ldots (24)$$

where $\mathbf{x} = \{x_{\text{t}}, x_{\text{comp}}, x_{\text{ctrl}}, x_{\text{jig}}\}^T$ is the vector of design variables, $C(\mathbf{x})$ are the design constraints, and N_L is the number of load cases.

It is worth mentioning that the optimisation studies are conducted via a sequential optimisation approach. For wings augmented by trailing-edge control surfaces, the first step is to find the optimal control scheduling that would yield minimum summation of the KS metrics for manoeuvre load cases M1 and M2. At this step, only control deflections are used as design variables. The second step (only applicable for composite wings) retains fixed optimal control deflections for load alleviation and minimises KS metrics for the most critical load case, this time using only lamination parameters as design variables. The final step handles all design variables simultaneously and minimises fuel burn as previously mentioned. This approach is not only useful in providing insight of the physical behaviours that govern the designs but also guarantees feasibility of the optimisation starting point. Moreover, it was found that this sequential optimisation technique solves the optimisation problem in a more

https://doi.org/10.1017/aer.2018.66 Published online by Cambridge University Press

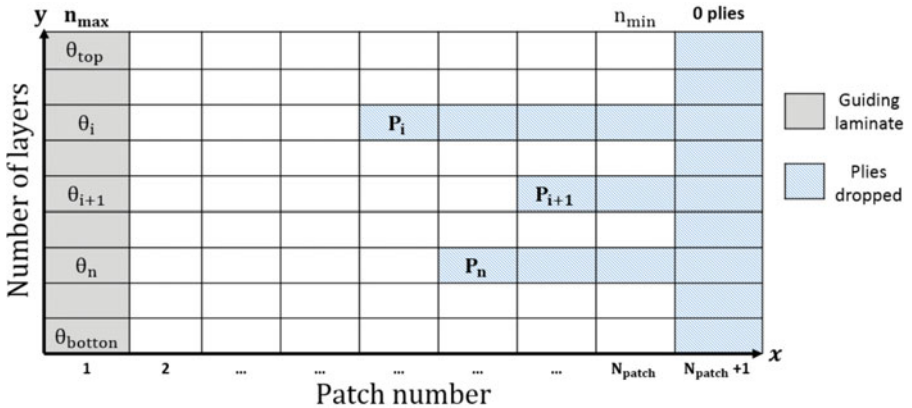


Figure 5. (Colour online) Rectangular coordinate system merged with an SST.

efficient manner, requiring fewer iterations to converge when compared to a random starting point, effectively searching the design space and yielding a better solution than the single step approach.

5.3 Bottom-level optimisation for stacking sequence retrieval for blended laminates

The stacking sequence retrieval of feasible laminates with blending considerations from lamination parameters is achieved by a separate bottom-level optimisation. This second level optimisation targets in-plane and out-of-plane lamination parameters and the thicknesses output from the top-level solution.

In this work, we propose an approach that combines the idea of *Stacking Sequence Tables* (SST) as proposed by Ref. 48 and the *guide-based blending* approach, first introduced in Ref. 49. Here, differently from Ref. 48 , SSTs are mapped into a Cartesian coordinate system as shown in Fig. 5. Starting from the thicker laminate (i.e. the guiding laminate), the "*x*-coordinate" denotes the wing skin patch number, while the "*y*-coordinate" represents the ply position relative to the laminate's mid-surface. These coordinates are restricted to the set of natural numbers ($\mathbb{N}$) only. As in Ref. 49, the panels' stacking sequences are derived from a thicker guiding stack by dropping off plies at specific locations within the laminate. In Fig. 5, each point P_i specifies a pair of numerical coordinates, which represent drop-off locations. From that point, a layer is removed from all thinner patches adjacent to the guide laminate.

The representation of a SST as a rectangular coordinate system allows the ply drop-offs x and y coordinates to be used as integer design variables along with the ply angles of the guiding laminate. The total number of design variables is $3n$ (n ply angles, n "x-coordinates", and n "y-coordinates"), where n represents the number of layers of the guide-laminate. The problem is constrained by the design guidelines developed in Section 4.2. For this bottom-level optimisation, we chose a particle swarm optimisation (PSO) algorithm, which produced attainable solutions at a reduced computational cost when compared to other evolutionary optimisation algorithms.

The objective function is a weighted sum of root square differences between the top-level lamination parameters and thicknesses $\xi^{A,D}_{j,\text{target}}$ and $t_{p,\text{target}}$, respectively, and the lamination

https://doi.org/10.1017/aer.2018.66 Published online by Cambridge University Press

parameters and thicknesses calculated at the n^{th} PSO iteration such that

$$f_{\text{obj}}^{\text{bottom-level}}(\bar{x}) = \alpha_1 \sqrt{\sum_{j=1}^{4} \left(\xi_j^{\text{A}} - \xi_{j,\text{target}}^{\text{A}}\right)^2} + \alpha_2 \sqrt{\sum_{j=1}^{4} \left(\xi_j^{\text{D}} - \xi_{j,\text{target}}^{\text{D}}\right)^2} + \alpha_3 \sqrt{\sum_{p=1}^{N_p} \left(t_p - t_{p,\text{target}}\right)^2}, \quad \ldots (25)$$

where the objective function is scaled to the order of unity by suitably choosing the weighting factors α_i, and N_p is the number of wing skin patches. In particular, it is found that $\alpha_1 = \alpha_2 = 0.275$ and $\alpha_3 = 0.45$ would yield reasonable results.

6.0 RESULTS DISCUSSION

This section contains the results obtained for six different design studies. In addition to those described in Table 3 (OPTs 1, 2, 3 and 4), here we discuss the aerostructural performance of the composite designs with stacking sequences retrieved with the second-level optimisation. We label these designs as *OPT 2 SSr* and *OPT 4 SSr*, respectively, where *SSr* stands for Stacking Sequence Retrieved.

Aerostructural performance benefits, in terms of load alleviation and fuel burn minimisation, of the composite wing with full-span trailing-edge controls are demonstrated by assessing the designs produced by the optimisation algorithm described in Section 5. Note that all the results presented are considered to be local optima, though different optimisation starting points did, in general, reveal similar trade-offs with minor variations in the objective function.

6.1 Composite stiffnesses

The out-of-plane lamination parameters obtained in the top-level optimisation for both the aeroelastically tailored and the aeroservoelastically tailored wings are shown in Fig. 7, along with the lamination parameters retrieved after blending constraints are applied. In-plane anisotropy is shown in Fig. 6 in terms of ply percentages (given by Equation (14)) distribution along the wing semi-span.

It is noted that both the upper and lower skins of OPT2 and OPT4 are mostly unbalanced featuring non-negligible values of $+45^\circ$ and ξ_2^D. These terms are respectively linked to the skins membrane and bending anisotropy. In general, both wings showed similar ply distributions with more 0° plies allocated towards the wing root (mostly at 20% of the semi-span) nearly reaching the upper bound of 60% with smoothly increasing amounts of $+45^\circ$ towards the wing tip. This design trend indicates that the solver effectively aligns ply directions with the wing load path and uses the bend-twist coupling as a passive means for inducing the washout mechanism, which alleviates the aerodynamic loads allowing for more material to be removed from the outer skins and spars. It is thought that -45° and 90° plies are mainly used to redistribute localised high strain areas at the spar breaks, particularly at the inner trailing-edge spar of OPT4 and at the edge between the outer front spar and lower wing skin of OPT2. Note that for most of the wing semi-span, there are a minimum number of -45° plies (10%).

https://doi.org/10.1017/aer.2018.66 Published online by Cambridge University Press

https://doi.org/10.1017/aer.2018.66 Published online by Cambridge University Press

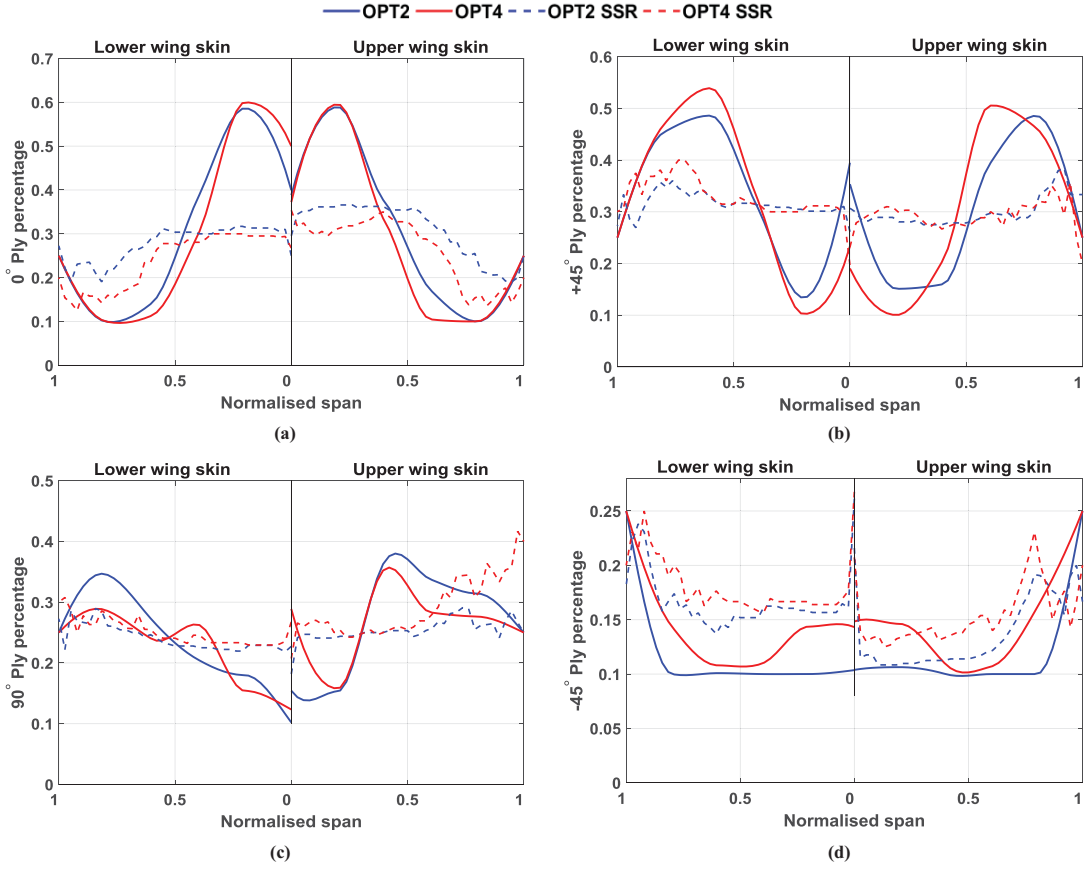


Figure 6. (Colour online) Optimised ply percentage distributions. (a) 0° plies. (b) +45° plies. (c) 90° plies. (d) −45° plies.

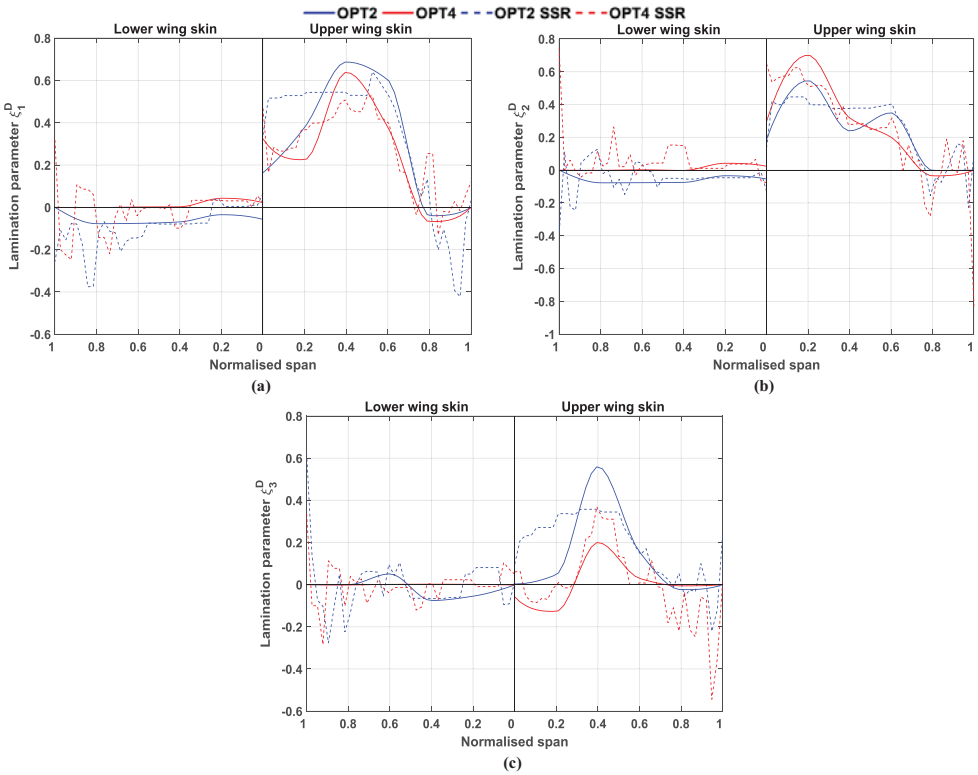


Figure 7. (Colour online) Optimised out-of-plane lamination parameters. (a) $\boldsymbol{\xi_1^D}$. (b) $\boldsymbol{\xi_2^D}$. (c) $\boldsymbol{\xi_3^D}$.

Upon further analysis it is observed that in comparison to the passively tailored skin of OPT2, OPT4 has greater shear-extension coupling inboard along the wing semi-span. This is evidenced for both upper and lower skins by the values of $+45^\circ$, which govern the laminate stiffnesses A_{16} and A_{26}. Similarly, after 20% of the semi-span, lower 0° ply percentages are found in the aeroservoelastically tailored composite wing. This result can be explained by the optimal control deflection scheduling for the symmetric 2.5 g manoeuvre shown in Fig. 12. The trailing-edge downwards rotations of the inner wing flaps move the local centre of pressure aft inducing a torque on the wingbox, which in turn shift torsional loads further inboard towards the wing semi-span. Though this difference is not substantial, it is thought that increasing control surface's area and/or control surface rotation would, presumably, enhance this effect compelling the optimiser to allocate additional $+45^\circ$ plies inboard the wing when compared to the passive counterpart.

Conversely, out-of-plane couplings (see Fig. 7) are stronger when adaptive control surfaces are not brought into the problem and are mainly used to improve the buckling strength in the wing root and mid-span areas. Inboard along the OPT2 wing, greater positive stiffnesses, linked to lamination parameters ξ_1^D and ξ_3^D, are observed for the upper wing skin. For both composites wings, buckling constraints of the lower skins are inactive so that the out-of-plane lamination parameters are mainly used to attain feasibility of Equation (13), which are found to be active for both skins.

https://doi.org/10.1017/aer.2018.66 Published online by Cambridge University Press

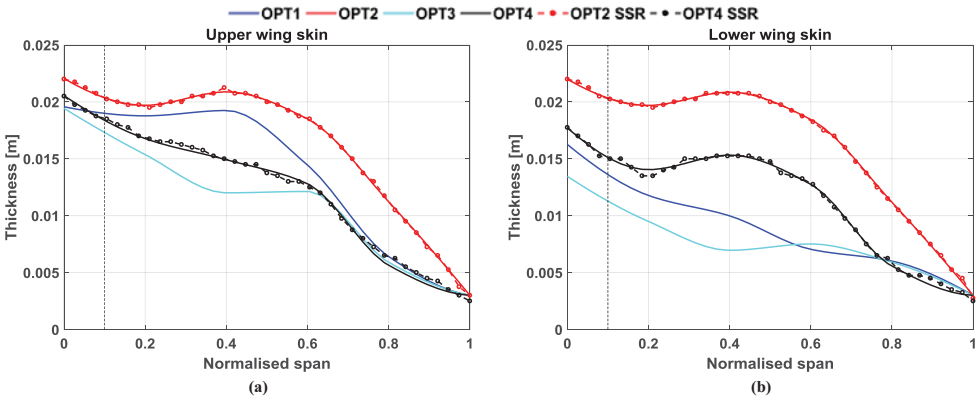


Figure 8. (Colour online) Optimised wing skin thickness distributions. (a) Upper wing skin thickness distribution. (b) Lower wing skin thickness distribution.

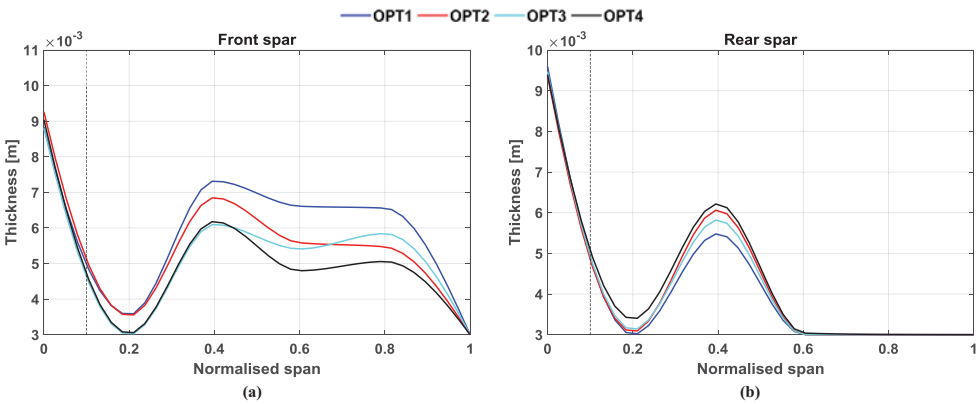


Figure 9. (Colour online) Optimised spars thickness distributions. (a) Front spar. (b) Rear spar.

The lamination parameters obtained from the bottom-level optimisation and corresponding to feasible stacking sequences with blending constraints applied show significant deviations from the target stiffnesses (obtained in the first-level optimisation). Nonetheless, the impact of these deviations on the overall structural response is limited and detailed in the remainder of this section.

6.2 Thickness and strain distributions

Optimised shell thicknesses for wing skins and spars are shown in Figs. 8 and 9. For all designs, the upper skins are thicker than the lower skins, indicating that the 2.5 g pull-up manoeuvre buckling constraint is a strong design driver. In comparison to the passive adaptive wings, both control-actuated designs have substantially thinner skins and spars, marking a considerable weight reduction. In general, skin peak thicknesses are achieved approximately at the wing root and at the innermost 40% of the semi-span. Comparing OPT2 and OPT4 upper skin thicknesses, one can note that substantial weight reduction was achieved mainly by removing material outboard the first 20% of the wing semi-span. A similar design trend is observed when comparing OPT1 and OPT3 cases. It is found that the thickness sizing for the

https://doi.org/10.1017/aer.2018.66 Published online by Cambridge University Press

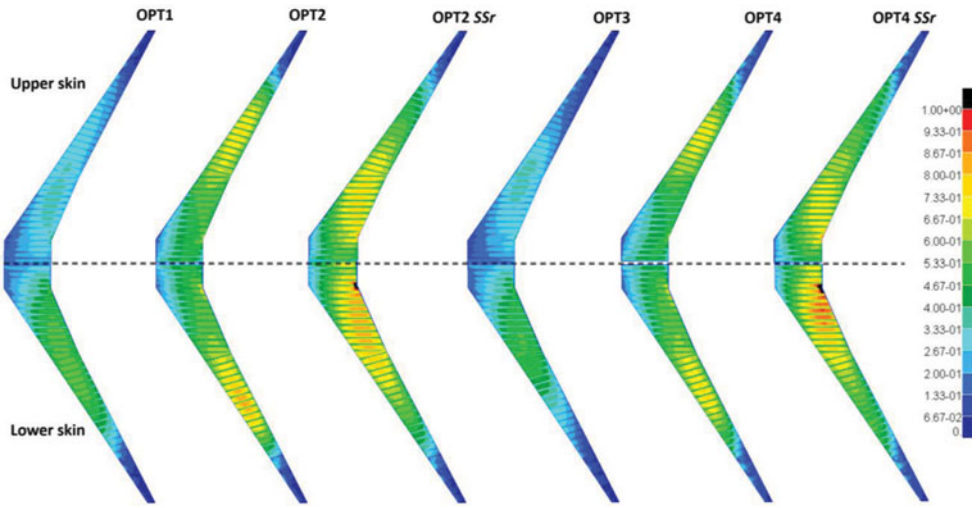


Figure 10. (Colour online) KS function for strain distribution.

metallic wings is mainly driven by active buckling constraints of the load cases M1 and M2, whereas for both composite wings, principal strains of the lower wing skin and 2.5 g pull-up manoeuvre buckling constraint are the main design drivers.

The thickness profiles for the rear spars in OPT3 and OPT4 are similar in magnitude and approximately constant after the wing Yehudi break location. Note that, in all the optimised solutions, heavier front spars than the rear spars were achieved, possibly due to 2.5 g torsional loads that induce higher stresses locally, with this being more evident for the spars of OPT1and OPT3. Moreover, the stiffer front spar creates a bend-twist coupling that induces a washout effect by shifting the flexural axis forward, further alleviating the wing loads. This effect is less prominent for the composite wing since it uses in-plane anisotropy on the skins to produce the same effect in a more efficient way.

The strain fields on upper and lower skins for the 2.5 g load case are shown in Fig. 10, in terms of normalised strains averaged through the shell thickness. Rib strains are, in general, homogenously small when compared to those developed in the skins and, thus, not shown here. Strain fields of the front and rear spars follow approximately the same distribution and magnitude of those observed at the edges of the skins, and similarly are not covered here. Overall, all designs have a strain distribution varying smoothly, with peak values occurring along the wingbox trailing-edge, especially at the fuselage-joint connection and in the wing kink areas. This effect is more evident at the mid semi-span, where the transition in rib orientation occurs. Note that for the composite designs, the KS constraints for principal strains are active in a few grid points of the fuselage-joint connection of the lower skin. Owing to the conservatism of the KS function, and to the fact that the normalised strains shown in Fig. 10 are averaged through the element thickness and grid points, the normalised active strain constraints are slightly less than 1.

The allowable strains for the composite skins are substantially lower than those for the all-metallic wings. Consequently, composite designs carry higher normalised strains values (of the order of $\sim$ 0.80 to 0.85). Due to a significant reduction in both shear-extension and bend-twist couplings, OPT2 SSr and OPT4 SSr operate in a more critical load state, where strain

https://doi.org/10.1017/aer.2018.66 Published online by Cambridge University Press

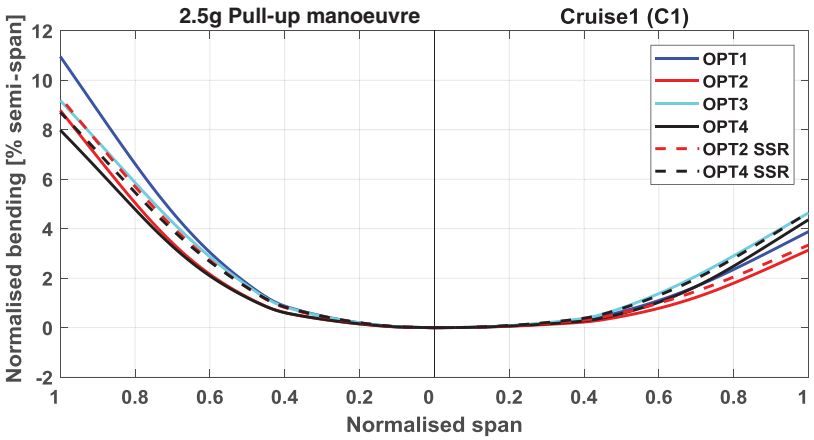


Figure 11. (Colour online) Bending deformations.

and buckling constraints are violated (approximately 5% higher than the maximum allowed), resulting in increased strains spread throughout a larger portion (shifted towards the wing root) of the wing skins. Furthermore, it is noted that there is a difference between some of the lamination parameters and ply percentages matching in Figs 6 and 7, suggesting that the changes in the root to mid-sections (up to 0.4 normalised wing span) are mostly responsible for the structural improvements.

In terms of deflections, Fig. 11 shows that wings actuated by controls deflect more at the cruise condition (C1) than the wings optimised without controls. For load relief, it is observed that both composite wings are less compliant in bending than the equivalent all-metallic wings. Comparing the composite wings and their respective second-level solution, although the influence on the displacement response appears small, the redistribution of strains from the first and second level design is quite important as shown in Fig. 10. This is a result already highlighted in previous studies[50,51].

6.3 Control deflections, span loads and twist shapes

In flexible wing structures (flying under the control reversal speed), the local lift generated by a streamwise section increases when the flaps are deflected downwards and decreases when upwards-control rotations are given. A tip-down flap increases the nose-down pitching moment about the wing aerodynamic centre, forcing the aircraft to reduce its trim angle-of-attack. Opposite behaviour is observed when a flap is rotated upwards. Generally, a flap deflection changes the aerofoil camber, thereby reshaping the aerodynamic loads and changing the spanwise drag and lift distributions.

Swept-back wings can be more sensitive to positive control deflections (flap rotated downwards), because the structural bend-twist coupling (that can be altered by laminate stiffnesses for the wing with composite skins) will naturally cause the wing to washout. Therefore, the resulting amount of nose-down twist will be the combination of those accompanied by the wing bending deflection and those due to the increase in pitching moment that further increases the wing torsion. This load redistribution can be beneficial from the structural standpoint, because it shifts the centre of pressure further inboard rather than outboard.

https://doi.org/10.1017/aer.2018.66 Published online by Cambridge University Press

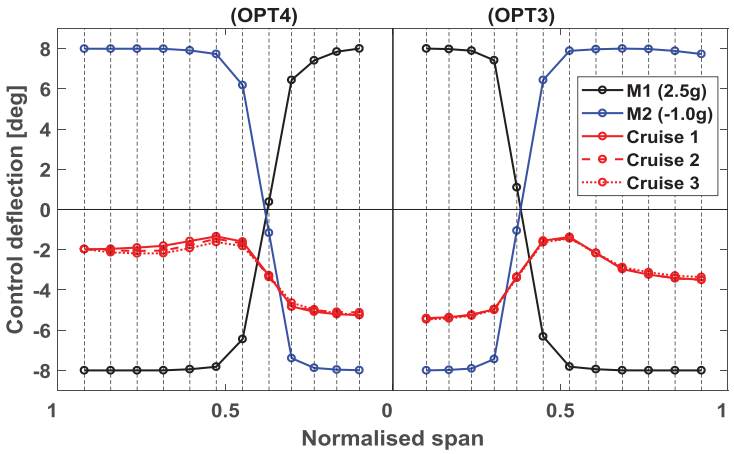


Figure 12. (Colour online) Optimised control surface deflections for cruise and manoeuvre load cases.

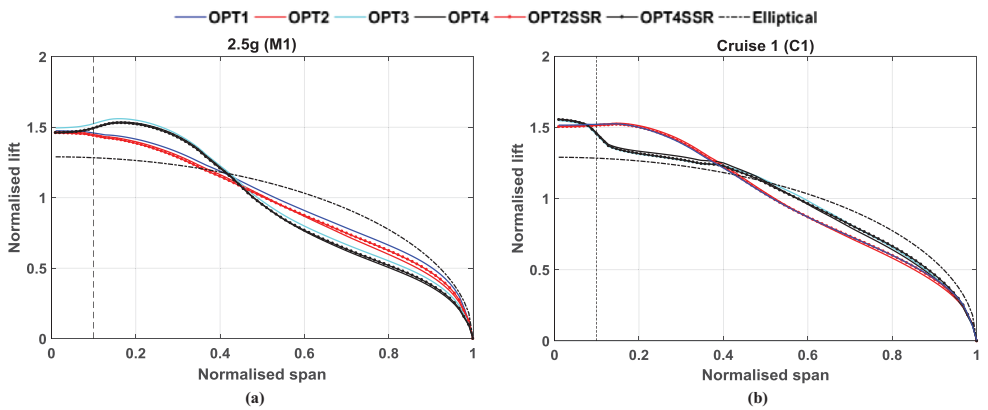


Figure 13. (Colour online) Cruise-climb and 2.5 g manoeuvre spanwise lift distributions for OPT1 through OPT4. (a) Spanwise lift distribution for manoeuvre load case. (b) Spanwise lift distribution for cruise 1 load case.

The control displacement layout found by the optimiser is shown in Fig. 12, for all of the cruise segments, along with the 2.5 g manoeuvre, and for both the wing with composite skins and the all-metallic structure. The main role played by the deflected controls during cruise alter the aerodynamic moments running spanwise along of the flexible wingbox, increasing the trim angle-of-attack (at constant lift coefficient) by producing more lift outboard, hence, reducing both wing drag and tailplane trim drag. Given the optimised jig-twist input variables and the resulting cruise twist distribution shown in Fig. 14, it is evident that for all of the design cases discussed here, the optimiser attempts to counteract the wing washout (due to the optimised jig-twist) by increasing the outboard streamwise angle-of-attack (wash-in) rotating the majority of the control surfaces upwards (negative deflection). The result is a lift distribution that reaches a more elliptical loading, as seen in Fig. 13, which would minimise the fuel burn.

In comparison to the all-metallic wing, the composite one needs less control deflections to achieve similar spanwise efficiency. This finding is thought to be due to the composite wing

https://doi.org/10.1017/aer.2018.66 Published online by Cambridge University Press

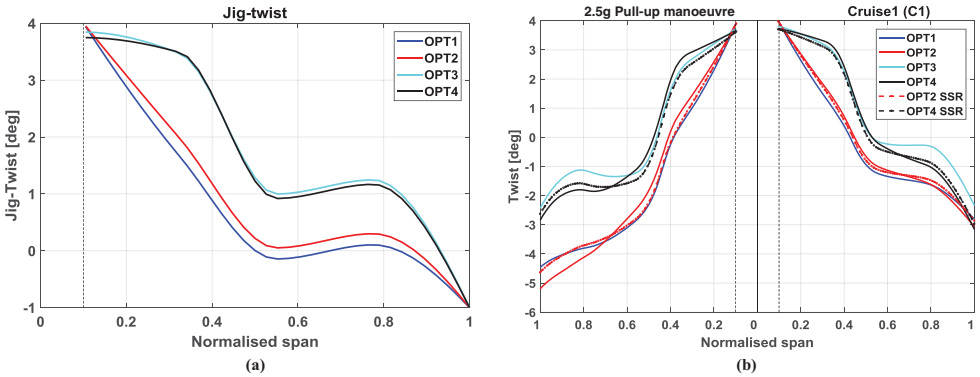


Figure 14. (Colour online) Jig-twist and elastic torsional deformations. (a) Jig-twist shape. (b) Elastic twist shape.

being more compliant in torsion; it requires a lower degree of wash-in to be produced by the trailing-edge flaps to "pull out" the triangular-shaped lift distribution to one closer to the elliptical shape.

Referring back to Fig. 12, showing the layout of the control displacements for the 2.5 g pull-up manoeuvre, one can assume that the optimiser uses negative control rotations outboard (control surface rotated upwards) to reduce the streamwise AoA locally, thus decreasing the amount of lift generated close to the wingtip. Since NASTRAN solution 144 performs a trim analysis, additional lift is then necessary for trimming the aircraft, which is achieved by giving the inner wing controls an upward displacement. This control deflection pattern is close to the one previously found by Stanford[26,27]. Intuitively, this loading shape is preferable from a structural perspective because the centre of pressure is shifted inboard, therefore reducing the root bending moment which, in turn, allows for more material to be removed from the wing skins and spars without any structural constraint violation.

Fuel burn, i.e. our objective function, does not depend entirely on aerodynamics with the total structural weight playing an important role in defining the optimal trade-offs between load alleviation and optimised cruise lift efficiency. This effect is shown by the optimised jig-twist shapes of Fig. 14(a), which, for all design cases, wash out approximately by 5° suggesting that the values for the jig-twist shape design variables are mainly dictated by manoeuvre buckling and strain constraints. In general, it is found that the optimised twist shape is set to alleviate loads via a passive washout mechanism, whereas the controls' displacements tend to increase lift outboard in order to reach the minimum-drag spanwise distribution.

Although normalised spanwise loads for the designs with retrieved blended laminates are almost identical to those obtained in the top-level optimisation, a small loss in aerodynamic performance is observed. This loss can be related to a small change in bending and twist deflections (due to smaller bend-twist couplings), that, in turn, degrade the aerodynamic performance due to increased trim drag.

6.4 Optimal wing weight and first-order performance implications

In this section, we examine and quantify the aerostructural performance of the design produced by the optimisation by assessing the total fuel burned (and the associated design metrics necessary for its calculation, e.g. wing structural mass and cruise lift efficiency)

https://doi.org/10.1017/aer.2018.66 Published online by Cambridge University Press

and by introducing a Payload-Range Efficiency parameter (PRE)[52]. Optimal design metrics are provided in Table 6 and benchmarked against OPT1 (all-metallic wing with undeflected control surfaces) which is the heaviest solution found. As expected, minimum fuel burn is achieved by simultaneously reducing wing structural mass and improving lift efficiency across the entirety of the cruise mission.

Higher lift-to-drag ratios are achieved by the optimisation studies that purposefully explore the use of controls to reshape the aerodynamic loads throughout cruising flight. Amongst the passively tailored designs, OPT2 features very similar L/D values when compared to OPT1, though less fuel burn is achieved as a result of the significant lighter structure (18.6% lighter). It is also noted that, for control-augmented designs, lift efficiency increases an average of approximately 4% for each cruise load case in comparison to the passive counterpart designs.

Wing structural mass (for half-aircraft, excluding leading-edge and trailing-edge lumped masses) is also shown in Table 6. One can note that including adaptive controls allows the optimiser to yield, for the all-metallic structure of OPT3, approximately 14% less structural weight than the reference design of OPT1. This difference is about 18% when considering the passive adaptive design of OPT2 and its counterpart, OPT4. Perhaps, greater mass reductions could be achieved if the wing skins were tailored in the chordwise direction as well, allowing for a more local tailoring. Additionally, it is thought that larger control surfaces operating at higher rotations or splitting the flaps into more chordwise and spanwise segments could yield higher lift efficiencies and would also improve weight savings.

Observing the last two rows of Table 6 and referring back to Fig. 10, one can conclude that the differences between designs in lamination parameter space and stacking sequence space result in a small to moderate loss in aerostructural performance. This outcome reinforces the argument that blending constraints should be included in the top-level optimisation.

In addition to fuel burn, another convenient way of judging the cruise performance of transport aircrafts is assessing PRE. This metric can be interpreted as the useful work done (payload $\times$ range) per unit mass of fuel consumed and is given according to

$$\text{PRE} = \text{payload} \times \text{range}/\text{fuel burned}. \quad \ldots (26)$$

For a fixed MTOW, the difference in wing mass with respect to OPT1 is converted into additional payload and used to estimate the PRE parameter. Overall, both fuel burn and PRE parameter demonstrates the superiority of composite materials over all-metallic airframes clearly, especially when adaptive controls are added to alleviate critical loads and maximise cruise performance showing an improvement in fuel burn of approximately 6.0% in comparison to the reference metallic wing.

It is observed that the optimisation problem studied here is highly non-convex in nature. One could therefore imagine that multiple local solutions could exist. Future work may address this issue by adopting a more robust optimisation approach to better define the optimisation starting point to retrieve global optima.

7.0 CONCLUSIONS

A series of aeroservoelastic wingbox designs is presented that exploit the synergies between passive shape adaptations achieved via elastic tailoring (i.e. variations in thicknesses, jig-twist and stiffnesses) and via adaptive trailing-edge flaps, for manoeuvre load alleviation and enhanced fuel efficiency. The baseline wing is representative of a long-range commercial airliner and features laminated wing skins and a metallic wingbox substructure. Optimisations

https://doi.org/10.1017/aer.2018.66 Published online by Cambridge University Press

https://doi.org/10.1017/aer.2018.66 Published online by Cambridge University Press

Table 6
Wing structural weight and first-order performance implications

		C_L/C_D for cruise load cases				
Design study	**W_{wing} (kg)**	**C1**	**C2**	**C3**	**Fuel burned (kg)**	**PRE (kg of payload × nmi/kg of fuel)**
OPT 1	9859 (ref.)	18.357 (ref.)	18.119 (ref.)	17.734 (ref.)	62324 (ref.)	2454 (ref.)
OPT 2	8023 (−18.6%)	18.345 (−0.1%)	18.089 (−0.2%)	17.672 (−0.3%)	61472 (−1.4%)	2794 (+13.8%)
OPT 3	8456 (−14.2%)	19.239 (+4.8%)	18.995 (+4.8%)	18.579 (+4.8%)	59155 (−5.1%)	2828 (+15.2%)
OPT 4	**6573 (−33.3%)**	**19.129 (+4.2%)**	**18.856 (−4.1%)**	**18.401 (−3.8%)**	**58600 (−6.0%)**	**3183 (+29.6%)**
OPT 2 SSr	8022 (−18.6%)	18.328 (−0.2%)	18.071 (−0.3%)	17.656 (−0.4%)	61522 (−1.3%)	2791 (+13.7%)
OPT 4 SSr	6589 (−33.1%)	19.159 (+4.4%)	18.813 (−3.8%)	18.369 (−3.6%)	58671 (−5.8%)	3310 (+29.4%)

are conducted using a bi-level approach, which integrates gradient-based and particle swarm algorithms in order to tailor the wing locally and retrieve manufacturable composite stacking sequences.

Both optimised composite designs are largely unbalanced with non-negligible membrane and bending anisotropy. It is further noted that the composite wing with trailing-edge controls exhibits greater in-plane anisotropy more inboard the wing semi-span in comparison to the passively tailored composite wing. In general, designs with retrieved blended laminates show a moderate loss in aerostructural performance associated with greater bending deflections that downgrade lift efficiency. This observation suggests the need of incorporating additional blending constraints in the top-level optimisation.

Since fuel burn does not depend entirely on the wing's aerodynamics, it is found that the jig-twist shape resulting from the optimisation introduces a passive washout mechanism to alleviate loads. Similarly, flaps are used to increase lift outboard, in order to attain the spanwise load distribution that minimises the overall drag. Opposite results are observed when optimising for load alleviation only, which causes the wing's centre of pressure to shift inboard, thereby reducing root bending moment and structural demands.

Amongst the results presented, as expected, the hybrid wing with composite skins and trailing-edge devices outperforms the all-metallic wings clearly both in terms of fuel burn or payload-range efficiency parameter.

This work has demonstrated the improvement of performance of aeroservoelastically tailored composite wings, over traditional designs. Considerable weight savings can be obtained due to manoeuvre load alleviation accompanied by improved lift efficiency (hence, fuel burn) over a realistic flight with multiple cruise conditions.

ACKNOWLEDGEMENTS

This research was supported by the Conselho Nacional de Desenvolvimento Científico e Tecnológico (CNPQ), under the Science Without Borders programme.

REFERENCES

1. BOEING. Current market outlook 2016–2035, Available from: http://www.boeing.com/resources/boeingdotcom/commercial/about-our-market/assets/downloads/cmo_print_2016_final.pdf.
2. Airbus. Global market forecast 2017–2036 growing horizons, Available from: http://www.airbus.com/content/dam/corporate-topics/publications/backgrounders/Airbus_Global_Market_Forecast_2017-2036_Growing_Horizons_full_book.pdf.
3. KHARINA, A. and RUTHERFORD, D. Fuel efficiency trends for new commercial jet aircraft: 1960 to 2014, *International Council on Clean Transportation*, August 2015, Washington, DC, US. Available from: http://www.theicct.org/.
4. IATA. *IATA Technology Roadmap Report*, 4th ed, June 2013.
5. SHIRK, M., HERTZ, T. and WEISSHAAR, T. Aeroelastic tailoring – Theory, practice, and promise, *J Aircr*, 1986, **23**, (1), pp 6-18.
6. WEISSHAAR, T. Aeroelastic tailoring of forward swept composite wings, *J Aircr*, 1981, **18**, (8), pp 669-676.
7. JUTTE, C. and STANFORD, B. Aeroelastic tailoring of transport aircraft wings: State-of-the-art and potential enabling technologies, NASA/TM-2014-218252, April 2014.
8. STANFORD, B., JUTTE, C. and WIESEMAN, C. Trim and structural optimization of subsonic transport wings using nonconventional aeroelastic tailoring, *AIAA J*, 2016, **54**, (1), pp 293-309.
9. JUTTE, C., STANFORD, B., WIESEMAN, C. and MOORE, J. Aeroelastic tailoring of the NASA common research model via novel material and structural configurations, 52nd Aerospace Sciences Meeting, AIAA SciTech Forum, National Harbor, Maryland, US, AIAA 2014-0598.

https://doi.org/10.1017/aer.2018.66 Published online by Cambridge University Press

10. DILLINGER, J., KLIMMEK, T., ABDALLA, M. and GÜRDAL, Z. Stiffness optimization of composite wings with aeroelastic constraints, *J Aircr*, 2013, **50**, (4), pp 1159-1168.
11. KENNEDY, G. and MARTINS, J. A comparison of metallic and composite aircraft wings using aerostructural design optimization, 12th AIAA Aviation Technology, Integration, and Operations (ATIO) Conference and 14th AIAA/ISSM, 17–19 September 2012, Indianapolis, Indiana, US.
12. KENWAY, G., KENNEDY, G. and MARTINS, J. Aerostructural optimization of the common research model configuration, 15th AIAA/ISSMO Multidisciplinary Analysis and Optimization Conference, AIAA AVIATION Forum, Atlanta, Georgia, US, AIAA 2014-3274.
13. KENWAY, G. and MARTINS, J. Multipoint high-fidelity aerostructural optimization of a transport aircraft configuration, *J Aircr*, 2015, **51**, (1), pp 144-160.
14. MARTINS, J., KENNEDY, G. and KENWAY, G. High aspect ratio wing design: Optimal aerostructural tradeoffs for the next generation of materials, 52nd Aerospace Sciences Meeting, AIAA SciTech Forum, National Harbor, Maryland, US, AIAA 2014-0596.
15. LIEM, R., KENWAY, G. and MARTINS, J. Multimission aircraft fuel-burn minimization via multipoint aerostructural optimization, *AIAA J*, 2015, **53**, (1), pp 104-122.
16. STANFORD, B. and JUTTE, C.V. Comparison of curvilinear stiffeners and tow steered composites for aeroelastic tailoring of aircraft wings, *Computer & Structures*, 2017, **183**, pp 48-60.
17. BROOKS, T., KENNEDY, G. and MARTINS, J. High-fidelity multipoint aerostructural optimization of a high aspect ratio tow-steered composite wing, 58th AIAA/ASCE/AHS/ASC Structures, Structural Dynamics, and Materials Conference, AIAA SciTech Forum, Grapevine, Texas, US, AIAA 2017-1350.
18. STODIEK, O., COOPER, J., WEAVER, P. and KEALY, P. Aeroelastic tailoring of a representative wingbox using tow-steered composites, *AIAA J*, 2017, **55**, (4), pp 1425-1439.
19. STANFORD, B. and DUNNING, P. Optimal topology of aircraft rib and spar structures under aeroelastic loads, *J Aircr*, 2015, **52**, (4), pp 1298-1311.
20. STANFORD, B. Aeroelastic wingbox stringer topology optimization, 18th AIAA/ISSMO Multidisciplinary Analysis and Optimization Conference, AIAA AVIATION Forum, Denver, Colorado, US, AIAA 2017-3655.
21. DUNNING, P., STANFORD, B. and KIM, A. Level-set topology optimization with aeroelastic constraints, AIAA SciTech Conference, 56th Structures, Structural Dynamics, and Materials Conference, 5–9 January 2015, Kissimmee, Florida, US, AIAA Paper 2015-1408.
22. FRANCOIS, G., COOPER, J. and WEAVER, P. Aeroelastic tailoring using rib/spar orientations: Experimental investigation, AIAA SciTech Conference, 56th Structures, Structural Dynamics, and Materials Conference, 5–9 January 2015, Kissimmee, Florida, US, AIAA Paper 2015-1408.
23. ZEILER, T. and WEISSHAAR, T. Integrated aeroservoelastic tailoring of lifting surfaces, *J Aircr*, 1988, **25**, (1), pp 76-83.
24. REGAN, C.D. and JUTTE, C.V. Survey of applications of active control technology for gust alleviation and new challenges for lighter-weight aircraft, Technical report, TM-2012-216008, NASA.
25. NGUYEN, N., LEBOFSKY, S., TING, E., KAUL, U., CHAPARRO, D. and URNES, J. Development of variable camber continuous trailing edge flap for performance adaptive aeroelastic wing, 2015, SAE Technical Paper 2015-01-2565.
26. STANFORD, B. Optimization of an aeroservoelastic wing with distributed multiple control surfaces, *J Aircr*, 2016, **53**, (4), pp 1131-1144.
27. STANFORD, B. Static and dynamic aeroelastic tailoring with variable-camber control, *J Guidance, Control, and Dynamics*, 2016, **39**, (11), pp 2522-2534.
28. STANFORD, B. Optimal control surface layout for an aeroservoelastic wingbox, *AIAA J*, 2017, **55**, (12), pp 4347-4356.
29. VASSBERG, J., DEHAAN, M., RIVERS, S. and WAHLS, R. Development of a common research model for applied CFD validation studies, 26th AIAA Applied Aerodynamics Conference, 10–13 August 2008, Honolulu, Hawaii, US.
30. KOLONAY, R. and EASTEP, F. Optimal scheduling of control surfaces on flexible wings to reduce induced drag, *J Aircr*, 2006, **43**, (6), pp 1655-1661.
31. DUKE, D. and WEISSHAAR, T. Induced drag reduction using aeroelastic tailoring with adaptive control surfaces, *J Aircr*, 2006, **43**, (1), pp 157-164.
32. LYU, Z. and MARTINS, J. Aerodynamic shape optimization of an adaptive morphing trailing-edge wing, *J Aircr*, 2015, **52**, (6), pp 1951-1970.

https://doi.org/10.1017/aer.2018.66 Published online by Cambridge University Press

33. RODRIGUEZ, D., AFTOSMIS, M., NEMEC, M. and ANDERSON, G. Optimization of flexible wings with distributed flaps at off-design conditions, AIAA SciTech Conference, 56th Structures, Structural Dynamics, and Materials Conference, 5–9 January 2015, Kissimmee, Florida, US, AIAA Paper 2015-1409.
34. ZHAO, W. and KAPANIA, R. BLP optimization of composite flying-wings with sparibs and multiple control surfaces, 2018 AIAA/ASCE/AHS/ASC Structures, Structural Dynamics, and Materials Conference, AIAA SciTech Forum, Kissimmee, Florida, US, AIAA 2018-2150.
35. BURDETTE, D., KENWAY, G. and MARTINS, J. Performance evaluation of a morphing trailing edge using multipoint aerostructural design optimization, AIAA SciTech Conference, 57th Structures, Structural Dynamics, and Materials Conference, 4–8 January 2016, San Diego, California, US, AIAA Paper 2016-0159.
36. BURDETTE, D., KENWAY, G. and MARTINS, J. Aerostructural design optimization of a continuous morphing trailing edge aircraft for improved mission performance, 17th AIAA/ISSMO Multidisciplinary Analysis and Optimisation Conference, AIAA Aviation, 13–17 June 2016, Washington, DC, US.
37. CORKE, T.C. *Design of Aircraft*, 2005, Pearson Education, Singapore.
38. JONES, R. *Mechanics of Composite Materials*, 1975, New McGraw-Hill, New York, New York, US.
39. TSAI, W., HALPIN, C. and PAGANO, J. *Composite Materials Workshop*, 1968, Technomic Publishing Co., Inc., Stamford, Connecticut, US, 2018, pp 223-253.
40. TSAI, W. and HAHN, H. *Introduction to Composite Materials*, 1980, Technomic Publishing Co., Inc., Stamford, Connecticut, US.
41. BAILIE, J., LEY, R. and PASRICHA, A. A summary and review of composite laminate design guidelines, Technical report NASA, NAS1-19347. Northrop Grumman-Military Aircraft Systems Division, 1997.
42. BLOOMFIELD, M., DIACONU, C. and WEAVER, P. On feasible regions of lamination parameters for lay-up optimisation of laminated composite structures, *Proceedings of Royal Soc. A*, 2009, **465**, (2104), pp 1123-1143.
43. LIU, D., TOROPOV, V., QUERIN, M. and BARTON, C. Bilevel optimisation of blended composite wing panels, *J Aircr*, 2011, **48**, pp 107-118.
44. ABDALLA, M., KASSAPOGLOU, , C. and GURDAL, Z. Formulation of composite laminate robustness constraint in lamination parameters space, 50th AIAA/ASME/ASCE/AHS/ASC/ Structures Dynamics, and Materials Conference, 4–7 May 2009, Palm Springs, California, US.
45. NOCEDAL, J. and S.J. Wright. *Numerical Optimization*, 2nd ed. Springer Series in Operations Research, 2006, Springer Verlag.
46. KREISSELMEIER, G. and STEINHAUSER, R. Systematic control design by optimizing a vector performance index, International Federation of Active Controls Symposium on Computer-Aided Design of Control Systems, 1979, Zurich, Switzerland.
47. POON, N.M.K. and MARTINS, J.R.R.A. An adaptive approach to constraint aggregation using adjoint sensitivity analysis, *Structures and Multidisciplinary Optimization*, 2007, **34**, (1), pp 61-73.
48. IRISARRI, F., LASSEIGNE, A., LEROY, F. and LE RICHE, R. Optimal design of laminated composite structures with ply drops using stacking sequence tables, *Composite Structures*, 2014, **107**, (1), pp 559-569.
49. ADAMS, D., WATSON, L., GÜRDAL, Z. and ANDERSON-COOK, C. Genetic algorithm optimization and blending of composite laminates by locally reducing laminate thickness, *Advances in Engineering Software*, 2004, **35**, (1), pp 35-43.
50. MACQUART, T., WERTER, N. and DE BREUKER, R. Aeroelastic tailoring of blended composite structures using lamination parameters, 57th AIAA/ASCE/AHS/ASC Structures, Structural Dynamics, and Materials Conference, San Diego, California, US, 2016, p 1966.
51. BORDOGNA, M.T., MACQUART, T., BETTEBGHOR, D. and DE BREUKER, R. Aeroelastic optimization of variable stiffness composite wing with blending constraints, 17th AIAA/ISSMO Multidisciplinary Analysis and Optimization Conference, Washington, DC, US, 2016, p. 4122.
52. NANGIA, R. Efficiency parameters for modern commercial aircraft, *The Aeronautical J*, August 2006, **110**, (1110), pp 495-510.

https://doi.org/10.1017/aer.2018.66 Published online by Cambridge University Press